Supplement of

Increasing Sensitivity to Soil Moisture Deficits Predominantly Intensifies Evapotranspiration Stress in a Greening China

Yuan Liu[1], Yong Wang[1,2], Yong Zhao[1,2], Shouzhi Chen[3], Longhao Wang[4,5], Wenjing Yang[6], Xing Li[1], Xinxi Li[7], Huimin Lei[8], Huanyu Chang[9], Jiaqi Zhai[1,2], Yongnan Zhu[1,2], Qingming Wang[1,2], and Ting Ye[10]

[1]State Key Laboratory of Simulation and Regulation of Water Cycle in River Basin, China Institute of Water Resources and Hydropower Research (IWHR), Beijing, 100038, China
[2]Key Laboratory of Water Safety for Beijing-Tianjin-Hebei Region of Ministry of Water Resources, China Institute of Water Resources and Hydropower Research (IWHR), Beijing, 100038, China
[3]College of Water Sciences, Beijing Normal University, Beijing, 100875, China
[4]Key Laboratory of Water Cycle and Related Land Surface Processes, Chinese Academy of Sciences, Beijing, 100101, China
[5]Institute of Geographic Sciences and Natural Resources Research, University of Chinese Academy of Sciences, Beijing, 100049, China
[6]National Centre for Groundwater Research and Training, Flinders University, Adelaide, SA 5001, Australia
[7]PowerChina Asia & Pacific, Power Construction Corporation of China, Beijing, 100038, China
[8]State Key Laboratory of Hydroscience and Engineering, Department of Hydraulic Engineering, Tsinghua University, Beijing, 100084, China
[9]Academy of Eco-civilization Development for Jing-Jin-Ji Megalopolis, Tianjin Normal University, Tianjin, 300387, China
[10]State Key Laboratory of Water Resources and Hydropower Engineering Science, Wuhan University, Wuhan, 430072, China

Correspondence to: Yong Wang (wangyong@iwhr.com)

Supplementary Texts

Text S1. Bayesian Memory Dynamic Linear Model to estimate time-varying sensitivity

We employ the Multivariate Dynamic Linear Model (MDLM) to ascertain the time-varying sensitivities of the ESI with respect to its own lags over the previous 1-5 periods, as well as to various external driving factors. The MDLM, an extension of the Dynamic Linear Model (DLM), comprises both an observation equation and a state evolution equation:

$$y_t = \mathbf{F}_t^T \boldsymbol{\theta}_t + v_t \tag{1a}$$
$$\boldsymbol{\theta}_t = \boldsymbol{G}\boldsymbol{\theta}_{t-1} + \mathbf{w}_t \tag{1b}$$

The model disaggregates the ESI time series observations (y_t) into three distinct components: the local/trend (subscript l), seasonal (subscript s), and regression (subscript r) elements. Correspondingly, the regressor vector ($\boldsymbol{F}_t$), state vector ($\boldsymbol{\theta}_t$, representing the sensitivity coefficients), and state evolution matrix ($\boldsymbol{G}$) are each comprised of three analogous components. The observation noise v_t, adheres to a Gaussian distribution with a mean of zero, while the state evolution noise $\mathbf{w}_t$, also conforms to a Gaussian distribution with a mean of zero and is independent from v_t.

$$\boldsymbol{F}_t = \begin{bmatrix} \boldsymbol{F}_l \\ \boldsymbol{F}_s \\ \boldsymbol{F}_{r,t} \end{bmatrix}, \boldsymbol{\theta}_t = \begin{bmatrix} \boldsymbol{\theta}_{l,t} \\ \boldsymbol{\theta}_{s,t} \\ \boldsymbol{\theta}_{r,t} \end{bmatrix}, \boldsymbol{G} = \begin{bmatrix} \boldsymbol{G}_l & 0 & 0 \\ 0 & \boldsymbol{G}_s & 0 \\ 0 & 0 & \boldsymbol{G}_r \end{bmatrix} \tag{2}$$

The local component is the mean and trend of the ESI, with

$$F_l = \begin{bmatrix} 1 \\ 0 \end{bmatrix}, \theta_{l,t} = \begin{bmatrix} \theta_{l1,t} \\ \theta_{l2,t} \end{bmatrix}, \boldsymbol{G}_l = \begin{bmatrix} 1 & 1 \\ 0 & 1 \end{bmatrix}$$

where $\theta_{l1,t}$ and $\theta_{l2,t}$ indicate the local mean and trend of ESI in the time t, respectively.

The seasonal component comprises a blend of three Fourier series representing seasonality, with frequencies at $\omega_1 = \frac{\pi}{6}, \omega_2 = \frac{\pi}{3}$, and $\omega_3 = \frac{2\pi}{3}$,

$$\boldsymbol{F}_s = \begin{bmatrix} \boldsymbol{F}_{s1} \\ \boldsymbol{F}_{s2} \\ \boldsymbol{F}_{s3} \end{bmatrix}, \boldsymbol{\theta}_{s,t} = \begin{bmatrix} \boldsymbol{\theta}_{s1,t} \\ \boldsymbol{\theta}_{s2,t} \\ \boldsymbol{\theta}_{s3,t} \end{bmatrix}, \boldsymbol{G}_s = \begin{bmatrix} \boldsymbol{G}_{s1} & 0 & 0 \\ 0 & \boldsymbol{G}_{s2} & 0 \\ 0 & 0 & \boldsymbol{G}_{s3} \end{bmatrix}$$

where

$$\boldsymbol{F}_{s(i)} = \begin{bmatrix} 1 \\ 0 \end{bmatrix}, \boldsymbol{\theta}_{s(i),t} = \begin{bmatrix} \theta_{s(i),1,t} \\ \theta_{s(i),2,t} \end{bmatrix}, \boldsymbol{G}_{s(i)} = \begin{bmatrix} \cos \omega_i & \sin \omega_i \\ -\sin \omega_i & \cos \omega_i \end{bmatrix}, i \in \{1,2,3\}$$

Based on historical data up to time step t, the expected value of the seasonal component at time $t + k$ can be represented by the sum of three cosine functions, each characterized by distinct frequencies, amplitudes, and phases.

$$\mathbb{E}[y_{s,t+k}|y_{s,1}, \dots, y_{s,t}] = \boldsymbol{F}_s^T \boldsymbol{\theta}_{s,t+k}$$
$$= \sum_{i=1}^{3} \boldsymbol{F}_{s(i)}^T \boldsymbol{G}_{s(i)}^k \boldsymbol{\theta}_{s(i),t}$$
$$= \sum_{i=1}^{3} \begin{bmatrix} 1 & 0 \end{bmatrix} \begin{bmatrix} \cos \omega_i k & \sin \omega_i k \\ -\sin \omega_i k & \cos \omega_i k \end{bmatrix} \begin{bmatrix} \theta_{s(i),1,t} \\ \theta_{s(i),2,t} \end{bmatrix} \tag{3}$$
$$= \sum_{i=1}^{3} A_{i,t} \cos (\omega_i k + \phi_{i,t})$$

where $A_{i,t}$ and $\phi_{i,t}$ represent the magnitudes and phases of the harmonic components, respectively. Both $A_{i,t}$ and $\phi_{i,t}$ are dictated by $\boldsymbol{\theta}_{s(i),t}$.

The regression component employs a set of independent variables $(x_1, x_2, \dots, x_p)$ to model their impact on the dependent variable y_t.

$$\boldsymbol{F}_{r,t} = [x_{1,t}, x_{2,t}, \dots, x_{p,t}]^T, \boldsymbol{G}_r = \boldsymbol{I}_p$$

where $\boldsymbol{I}_p$ is the identity matrix of dimension p. The set of independent variables comprises the deseasonalized and detrended anomalies of the ESI from the preceding five time periods (Lag1~Lag5), as well as the anomalies of the driving factors for the current time step. These deseasonalized and detrended ESI anomalies are derived by applying a DLM devoid of regression elements, effectively eliminating the

trend and seasonal fluctuations from the ESI time series. The terms Lag1~Lag5 refer to the cumulative average of the respective preceding time periods. Specifically, Lag1 corresponds to the immediate prior interval, encompassing the past 8 days; Lag2 covers the time span from 8 to 16 days prior, exclusive of Lag1; and so forth. Consideration is limited to Lag1 through Lag5 because the impact of more distant time periods is deemed sufficiently minimal to warrant exclusion.

To address the aforementioned MDLM, we employed a technique known as forward filtering. This approach is conceptually akin to Kalman Filtering but incorporates an extra step to retroactively refine the posterior estimate of y_t in order to derive the posterior estimate of $\boldsymbol{\theta}_t$. Initially, we presuppose that the variances of the noise components v_t and $\mathbf{w}_t$ are predetermined.

(1) Posterior at $t-1$. Given all observations $D_{t-1} = \{y_1, y_2, \ldots, y_{t-1}\}$, $\boldsymbol{\theta}_{t-1}$ is assumed to follow a multivariate normal distribution:

$$\boldsymbol{\theta}_{t-1}|D_{t-1} \sim N(\boldsymbol{m}_{t-1}, \boldsymbol{C}_{t-1}) \tag{4}$$

where $\boldsymbol{m}_{t-1}$ is the predicted mean, and $\boldsymbol{C}_{t-1}$ is the variance matrix.

(2) Prior at t. Together with Eq. 2, we can get the prior distribution of $\boldsymbol{\theta}_t$,

$$\boldsymbol{\theta}_t|D_{t-1} \sim N(\boldsymbol{a}_t, \boldsymbol{R}_t) \tag{5}$$

where

$$\boldsymbol{a}_t = \boldsymbol{G}_t \boldsymbol{m}_{t-1}, \boldsymbol{R}_t = \boldsymbol{G}_t \boldsymbol{C}_{t-1} \boldsymbol{G}_t^T + \boldsymbol{W}_t$$

(3) One step forecast. Together with Eq. 1, the predictive distribution of y_t is

$$y_t|D_{t-1} \sim N(f_t, q_t) \tag{6}$$

where

$$f_t = \boldsymbol{F}_t^T \boldsymbol{a}_t, q_t = \boldsymbol{F}_t^T \boldsymbol{R}_t \boldsymbol{F}_t + v_t$$

(4) Posterior at t. Compared with the observed y_t, the posterior estimate of $\boldsymbol{\theta}_t$ based on all observations up to time t is derived using Bayes' rule:

$$p(\boldsymbol{\theta}_t|D_t) = p(\boldsymbol{\theta}_t|y_t, D_{t-1}) \propto p(\boldsymbol{\theta}_t|y_t, D_{t-1})p(y_t|\boldsymbol{\theta}_t, D_{t-1}) = N(\boldsymbol{m}_t, \boldsymbol{C}_t) \tag{7}$$

with

$$\boldsymbol{m}_t = \boldsymbol{a}_t + \boldsymbol{A}_t e_t, \boldsymbol{C}_t = \boldsymbol{R}_t - q_t \boldsymbol{A}_t \boldsymbol{A}_t^T$$

where

$$e_t = y_t - f_t, \boldsymbol{A}_t = \boldsymbol{R}_t \boldsymbol{F}_t/q_t$$

Here, $\boldsymbol{A}_t$ is the matrix of adaptive coefficients, e_t represents the one-step forecast errors. When y_t is missing due to cloud or snow, the prior from historical data $p(\boldsymbol{\theta}_t|D_{t-1})$ from Eq. 4 is used to estimate $\boldsymbol{\theta}_t$.

In practice, the variance of noise v and $\boldsymbol{W}_t$ are unknown. Consequently, we have refined the process for variance estimation. Initially, we posit that $v_t \sim N(0, v)$ and $\mathbf{w}_t \sim N(0, v\boldsymbol{W}_t^*)$. Both v and $\boldsymbol{W}_t^*$ are unknown parameters, with $\boldsymbol{W}_t^*$ being a rescaled version of $\boldsymbol{W}_t$. Given v, Eqs. 4-7 adheres to a consistent format,

$$\boldsymbol{\theta}_{t-1}|D_{t-1}, v \sim N(\boldsymbol{m}_{t-1}, v\boldsymbol{C}_{t-1}^*) \tag{8}$$
$$\boldsymbol{\theta}_t|D_{t-1}, v \sim N(\boldsymbol{a}_t, v\boldsymbol{R}_t^*) \tag{9}$$
$$y_t|D_{t-1}, v \sim N(f_t, vq_t^*) \tag{10}$$
$$\boldsymbol{\theta}_t|D_t, v \sim N(\boldsymbol{m}_t, v\boldsymbol{C}_t^*) \tag{11}$$

We assume the variation of observational error (v) follows an inverse-gamma (IG) distribution,

$$v|D_{t-1} \sim IG(n_{t-1}/2, d_{t-1}/2) \tag{12}$$
$$v|D_t \sim IG(n_t/2, d_t/2) \tag{13}$$
$$n_t = n_{t-1} + 1$$
$$d_t = d_{t-1} + e_t^2/q_t^*$$

where n_t is the degree of freedom, and

$$\boldsymbol{\theta}_{t-1}|D_{t-1} \sim T(\boldsymbol{m}_{t-1}, s_{t-1}\boldsymbol{C}_{t-1}^*) \tag{14}$$
$$\boldsymbol{\theta}_t|D_{t-1} \sim T(\boldsymbol{a}_t, s_{t-1}\boldsymbol{R}_t^*) \tag{15}$$
$$y_t|D_{t-1} \sim T(f_t, s_{t-1}q_t^*) \tag{16}$$
$$\boldsymbol{\theta}_t|D_t \sim T(\boldsymbol{m}_t, s_t\boldsymbol{C}_t^*) \tag{17}$$
$$s_{t-1} = d_{t-1}/n_t$$
$$s_t = d_t/n_t$$

We estimate $\boldsymbol{W}_t$ using a discounting approach. Based on Eq. 5, the prior variance of $\boldsymbol{\theta}_t$ as $Var(\boldsymbol{\theta}_t| = D_{t-1}) = \boldsymbol{R}_t = \boldsymbol{G}_t \boldsymbol{C}_{t-1} \boldsymbol{G}_t^T + \boldsymbol{W}_t = \boldsymbol{P}_t + \boldsymbol{W}_t$, where $\boldsymbol{P}_t$ is the variance without stochastic noise, that is, $\boldsymbol{W}_t = 0$. If $\boldsymbol{W}_t \neq 0$, we assert that $\boldsymbol{R}_t = \boldsymbol{P}_t/\delta$, with the parameter $\delta \in (0,1]$. This indicates that stochastic noise leads to an inflation of the variance by a factor of $\frac{1}{\delta} - 1$ at each step, correspondingly diminishing the

degrees of freedom from n_t to δn_t. Consequently, a smaller δ incurs more significant fluctuations in $\boldsymbol{\theta}_t$, and the inverse is true. To ensure the stability of local trends and seasonal components, minimally influenced by anomalies, we employ diverse δ values, selected through a grid search algorithm from the set [0.97,0.98,0.99,0.995,0.999]. We initialize the model at time step 0 using non-informative priors $\boldsymbol{m}_0 = 0, \boldsymbol{C}_0 = \boldsymbol{I}, n_0 = p, d_0 = 0.2^2 n_0$, permitting the parameter $\boldsymbol{\theta}_t$ to fluctuate freely initially and then gradually converge with the accumulation of more observations. To mitigate the effects of the initial substantial fluctuation and facilitate a gradual convergence of variance, we employ the first five years of ESI and drivers' data twice in a preparatory phase known as the "spin-up" period.

The model parsing process, influenced by Bayesian updating and Markov assumptions, introduces error terms and noise, necessitating the optimization of the δ value(Simoen et al., 2013; Zhang et al., 2011). For each pixel, the original sequence is partitioned into a training set and a validation set with an 80:20 ratio. Subsequently, we compute the coefficient of determination (R^2), root mean square error (RMSE), and mean absolute error (MAE) by comparing the original ESI sequence with the aggregate of the three components post-MDLM decomposition for both segments. This approach facilitates the evaluation of MDLM's precision in deconstructing and tracking the influence and reaction of evolving environmental conditions on evaporation stress (Fig. S10 for verification results).

Supplementary Figures
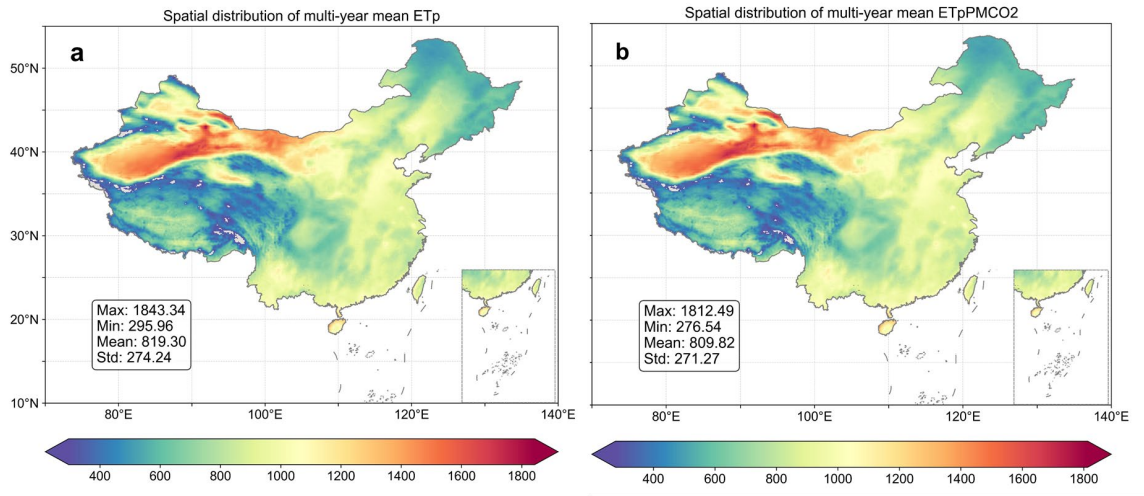
Figure S1. Comparison of the spatial distribution of the multi-year average potential evapotranspiration (ETp). (a) calculated by the traditional Penman-Monteith equation and (b) the modified Penman-Monteith equation that incorporates the CO_2 water-saving effect. The maximum value, minimum value, and average value are marked in the lower left corner of the figure.
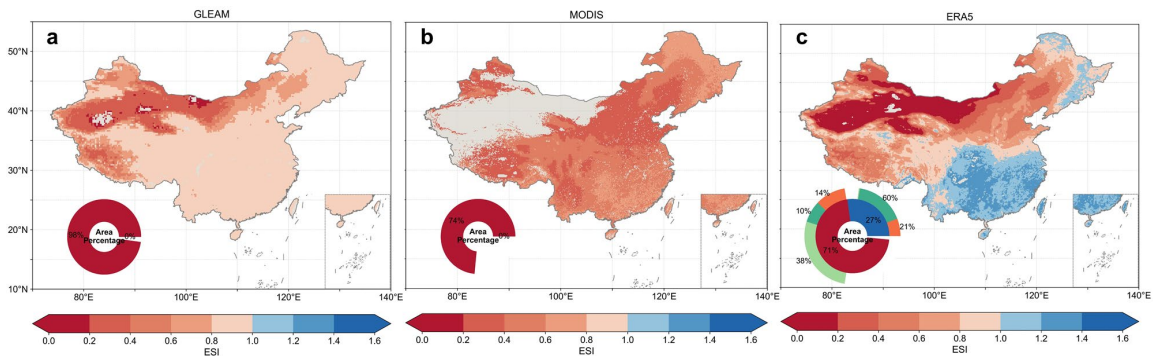
Figure S2. Spatial distribution of the multi-year average of ESI calculated from ETa and ETp products from different datasets. Panel a originates from GLEAM, panel b from MODIS, and panel c from ERA5. The ETp calculations for MODIS and ERA5 utilize the traditional Penman-Monteith (PM) formula tailored for specific ideal vegetation types, aligning more closely with the mechanistic hypothesis depicted in Fig. 1, which outlines the hydrology-climate-vegetation balance relationship. Conversely, GLEAM data incorporate considerations for the diversity of actual vegetation types.
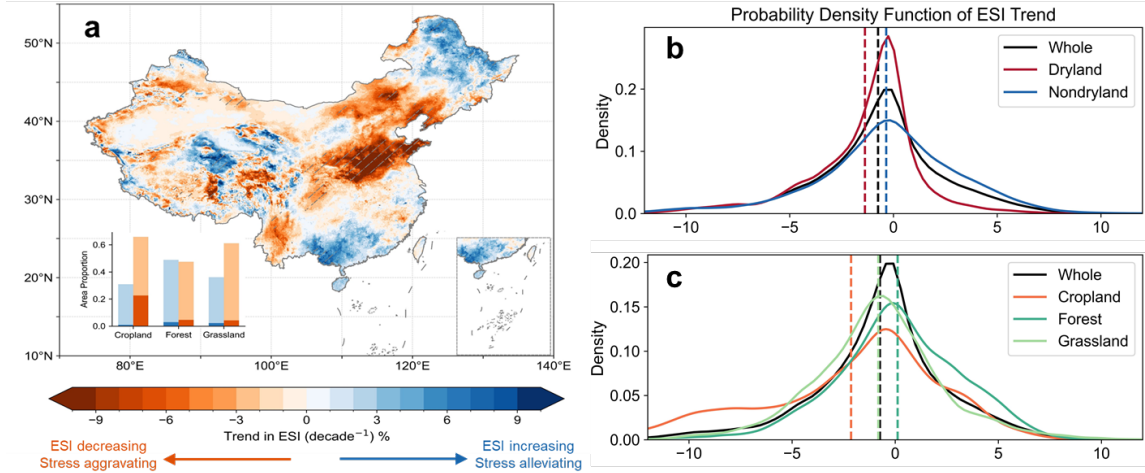
Figure S3. Spatial distribution of the tendency in ESI over the past 20 years. Same as Figs. 4cde in the main text, but ESI is calculated based on ETp that takes into account the CO_2 effect, with the time span from 2001 to 2020.
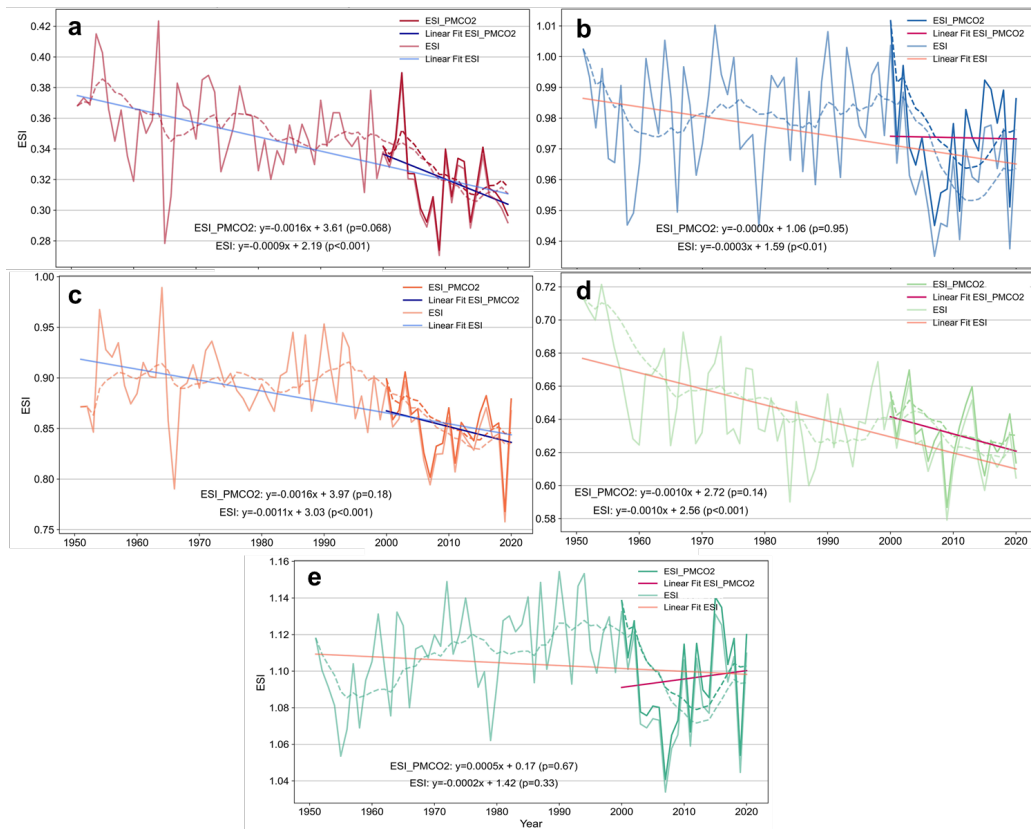
Figure S4. Time series and linear fitting of the regional average ESI. Same as Fig. 4a, but here it is for different climate zones and land use types, where (a) is dryland, (b) is non-dryland, (c) is cropland, (d) is grassland, and (e) is forest.
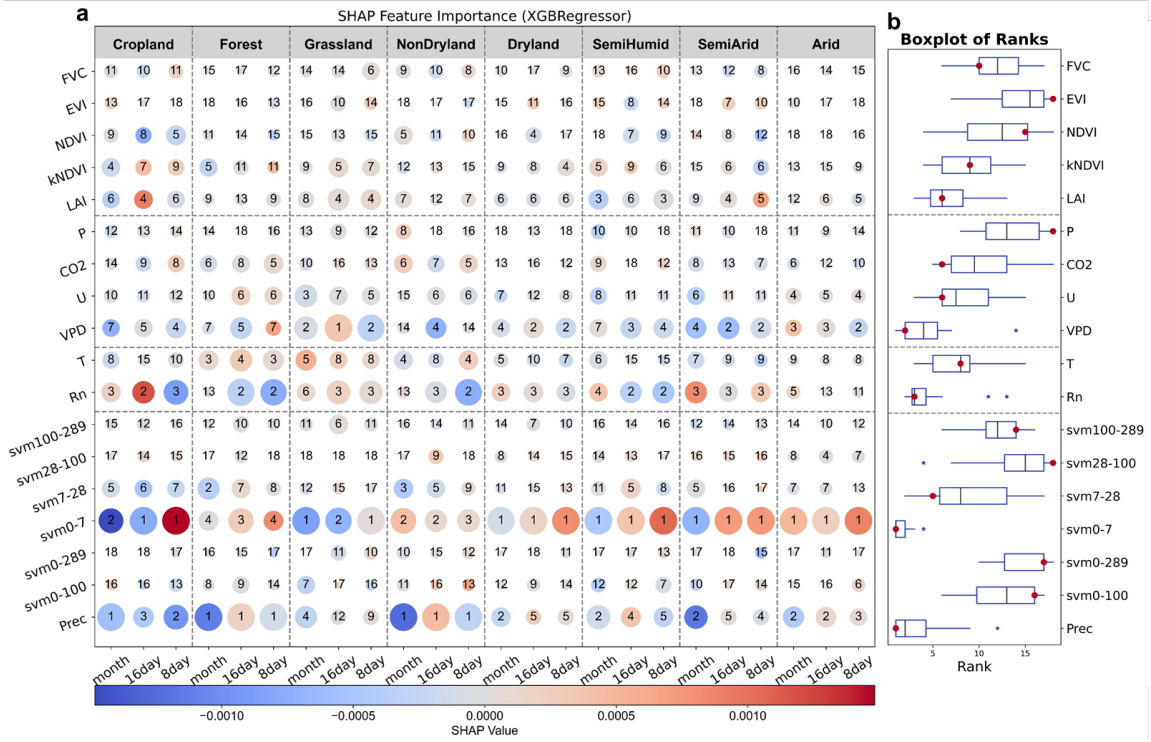
Figure S5. Identification of the key external drivers of ESI. Same as Fig. 5, but applying the XGBoost regressor. It is consistent with the overall results identified by the RF classifier, except that it fails to distinctly differentiate between surface soil moisture and precipitation.
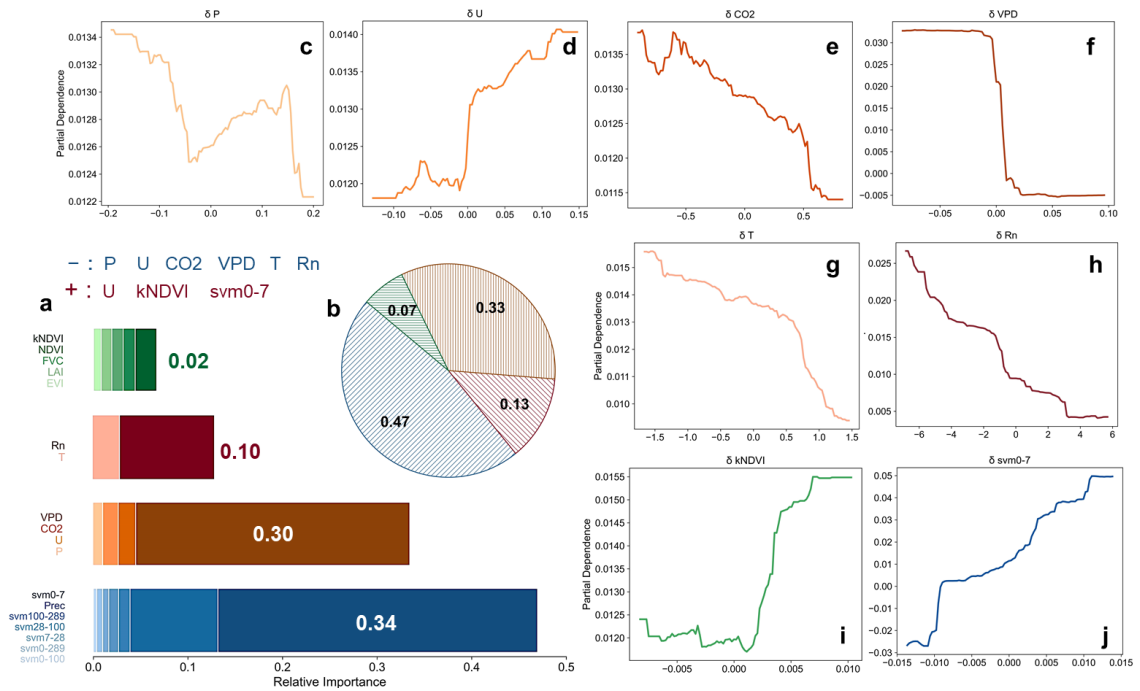
Figure S6. Importance and partial dependence of external drivers influencing ESI. Same as Fig. 6, but here examines the 16-day temporal resolution. The hierarchy of importance is as follows: water, climate, energy, and then vegetation. Compared to the 8-day temporal resolution findings, the importance of water and

vegetation factors remains virtually unchanged, with SVM0-7, VPD, and Rn as the most influential variables within their respective categories. However, kNDVI now stands out as the most effective metric for vegetation. The interdependencies between critical factors align closely with those identified in the 8-day interval analysis, yet the monotonic influence of CO_2 on the system appears to be more pronounced.
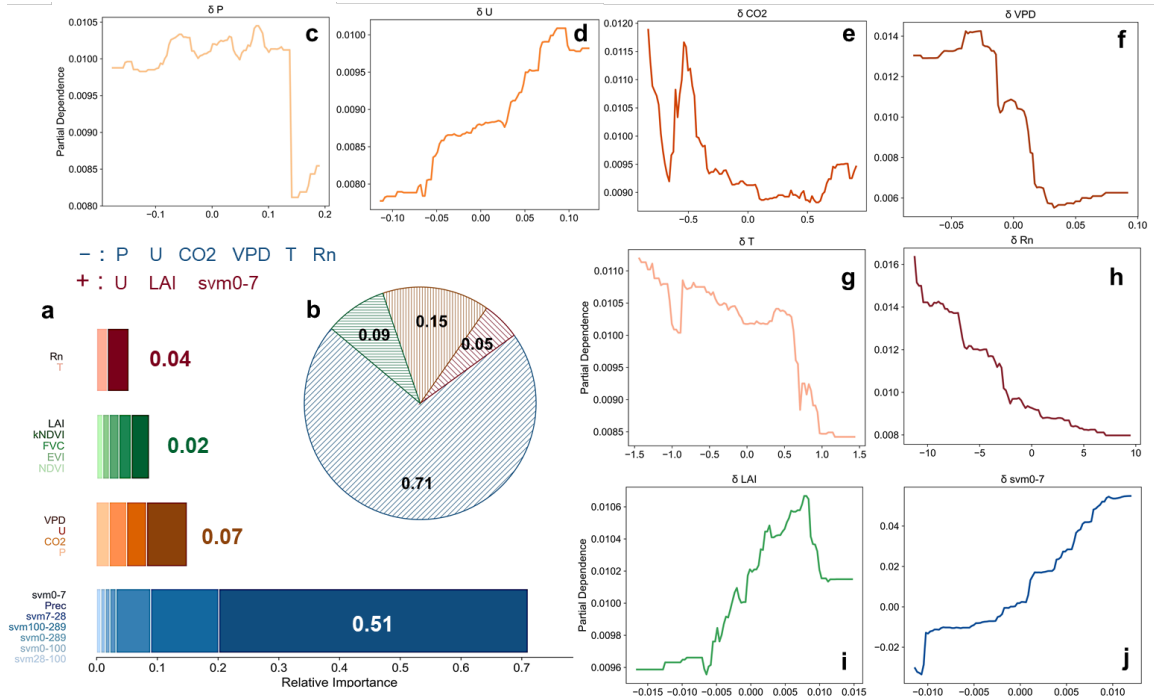
Figure S7. Importance and partial dependence of external drivers influencing ESI. Same as Fig. 6 & S6, but here analyze monthly series data. The order of importance is water > climate > vegetation > energy. Compared to the results from the 8-day and 16-day temporal results, the significance of water is amplified (with an increase to 0.71), whereas the contributions of meteorological and energy factors are diminished, with the latter being particularly affected. Factors such as SVM0-7, VPD, LAI, and Rn continue to be the most influential within their respective categories, aligning with observations from the 8-day temporal scale. The dependency direction of the pivotal factor aligns with that of the other two temporal dimensions. It is essential to note, however, that apart from Rn, an escalation in temporal scale granularity generally results in a decrease in the linearity and monotonicity of the Partial Dependence Plots (c-j) for the variables. It can be ascribed to the intricate interactions introduced by data averaging, or the distortion effects of noise, which tend to obscure the relationship.
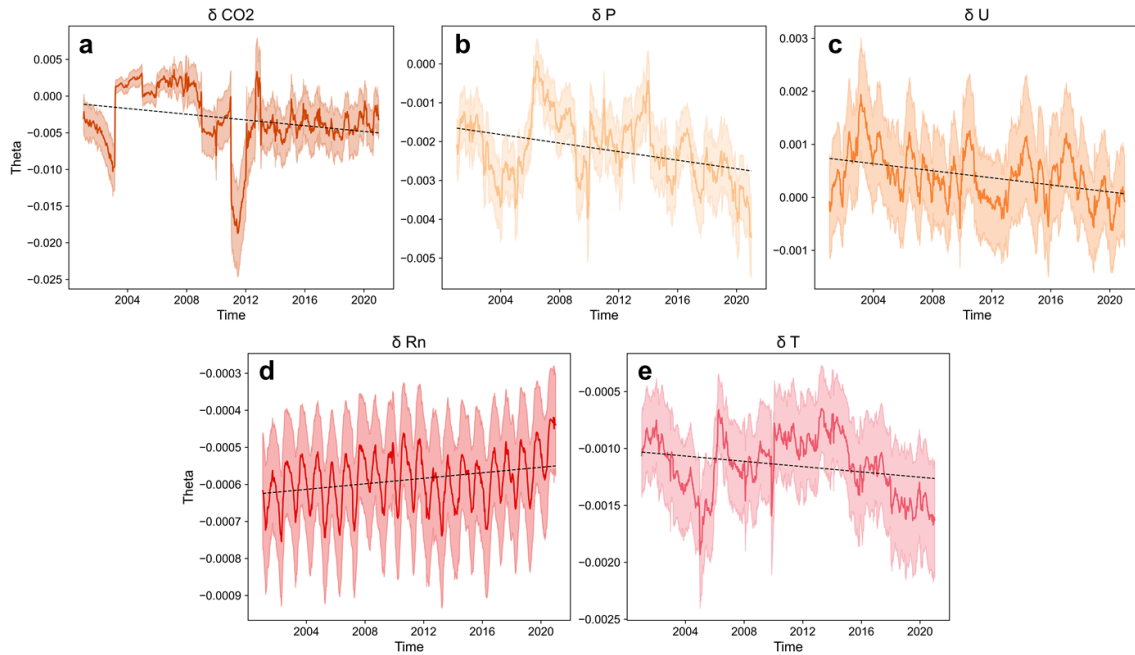
Figure S8. Sensitivity of the ESI to pivotal external drivers and its dynamic trajectory. Consistent with Figs. 7c-e, time series graphs are presented illustrating the sensitivity of CO_2 (a), atmospheric pressure-P (b), wind speed-U (c), net radiation-Rn (d), and temperature-T (e). The sensitivity values and trends of these factors are 1-2 orders of magnitude smaller than those for svm, VPD, and LAI, which are not elaborated upon in the main text. It is noteworthy that Rn, despite its lower sensitivity value, displays a marked annual cyclical pattern and an upward trend in sensitivity. In contrast, the remaining four variables exhibit an overall downward trend.
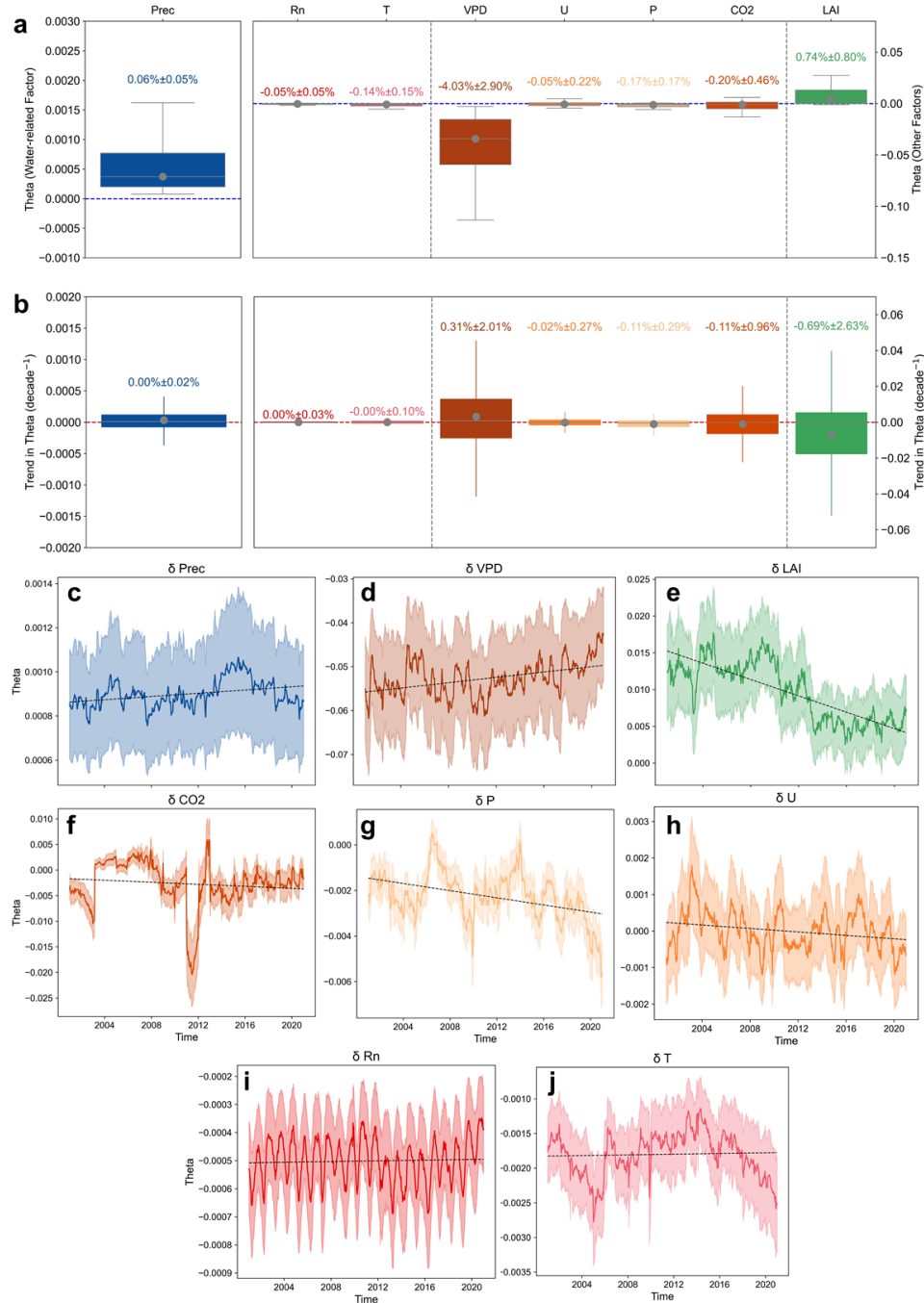
Figure S9. Sensitivity of the ESI to pivotal external drivers and its dynamic trajectory. Same as Figs. 7 & S8, but here the MLDM model, encompassing lag1-5, was used to establish the sensitivity profile for the following external factors: Precipitation -Prec, Rn, T, VPD, U, CO_2, and LAI (Parameter Set: R1). It was discerned that ESI exhibits considerably lower sensitivity to precipitation than to soil water (0.06% vs 1.30%). The sensitivity of additional factors displayed a consistent pattern in both magnitude and directional trend, with a slight uptick in values, potentially attributable to the limited role of Prec in explaining ESI compared to svm. The observed trend aligns with the R0 scenario that incorporates soil water input, thereby corroborating the robustness of research findings. These findings indicate heightened sensitivity to both water supply and VPD, coupled with a diminished sensitivity of LAI.
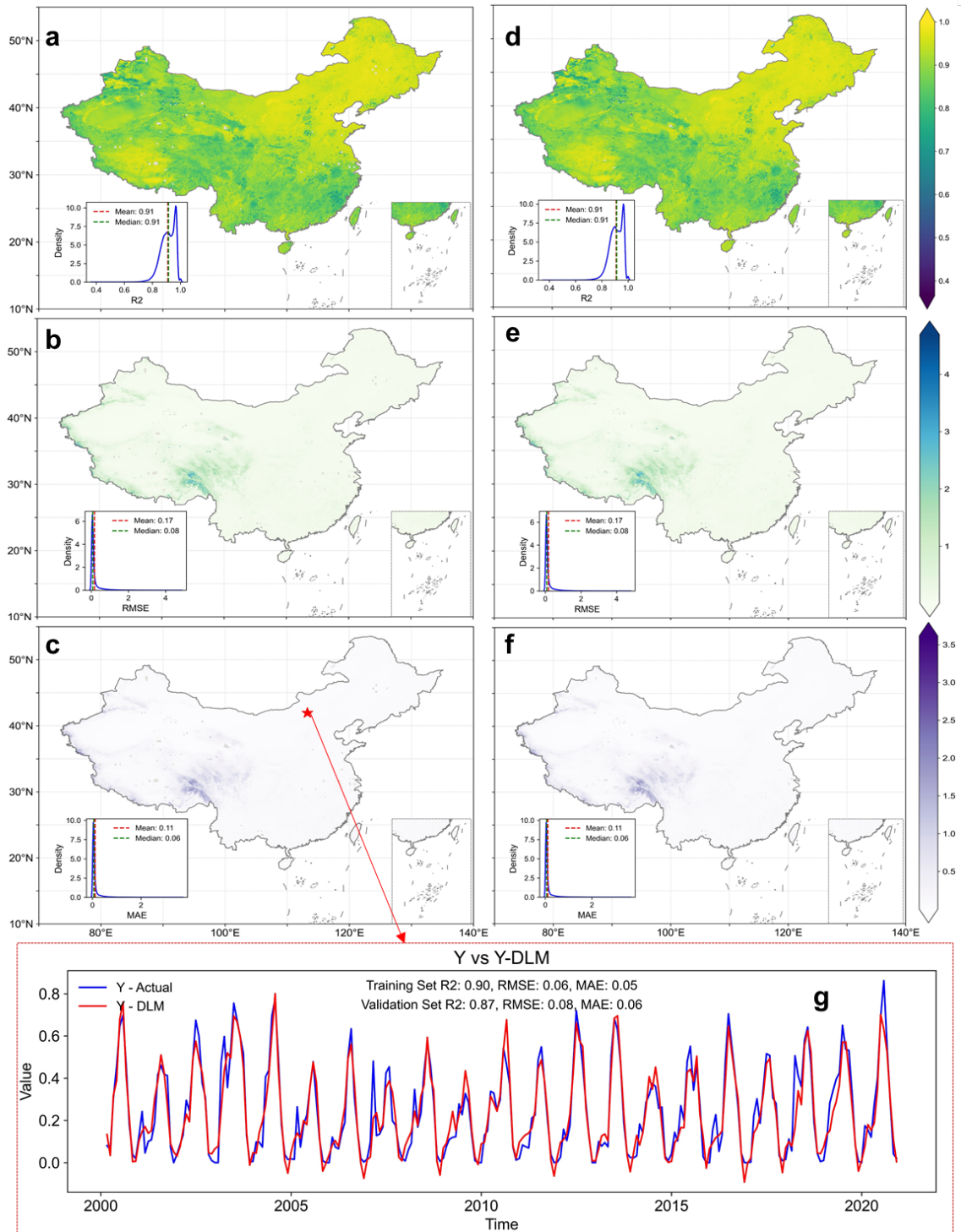
Figure S10. Simulation accuracy and validation of the MDLM model. For each pixel, simulations were conducted using two distinct parameter sets, R0 and R1. The dataset was partitioned into a training set and a validation set at a ratio of 8:2, facilitating the evaluation of the model's ability to accurately fit the actual ESI sequence, along with its local, seasonal, and trend components. This process is exemplified through the analysis of a single pixel in (g), with the method detailed in Text S1. (a-c) The distribution of the R^2, RMSE, and MAE for the validation set, with R0 parameter set. These figures include insets that show the

distributions across the region, with the mean and median values delineated by red and green dashed lines, respectively. (d-f) The model's performance using the R1 parameter set. The analyses reveal that the MDLM model achieves a consistently high fitting accuracy with both parameter sets, evidenced by an average R^2 of 0.91, an RMSE of 0.17, and an MAE of 0.11. It is noted that results exhibit suboptimal performance in specific regions of the Tibetan Plateau, however, remain relatively high credibility in other areas.
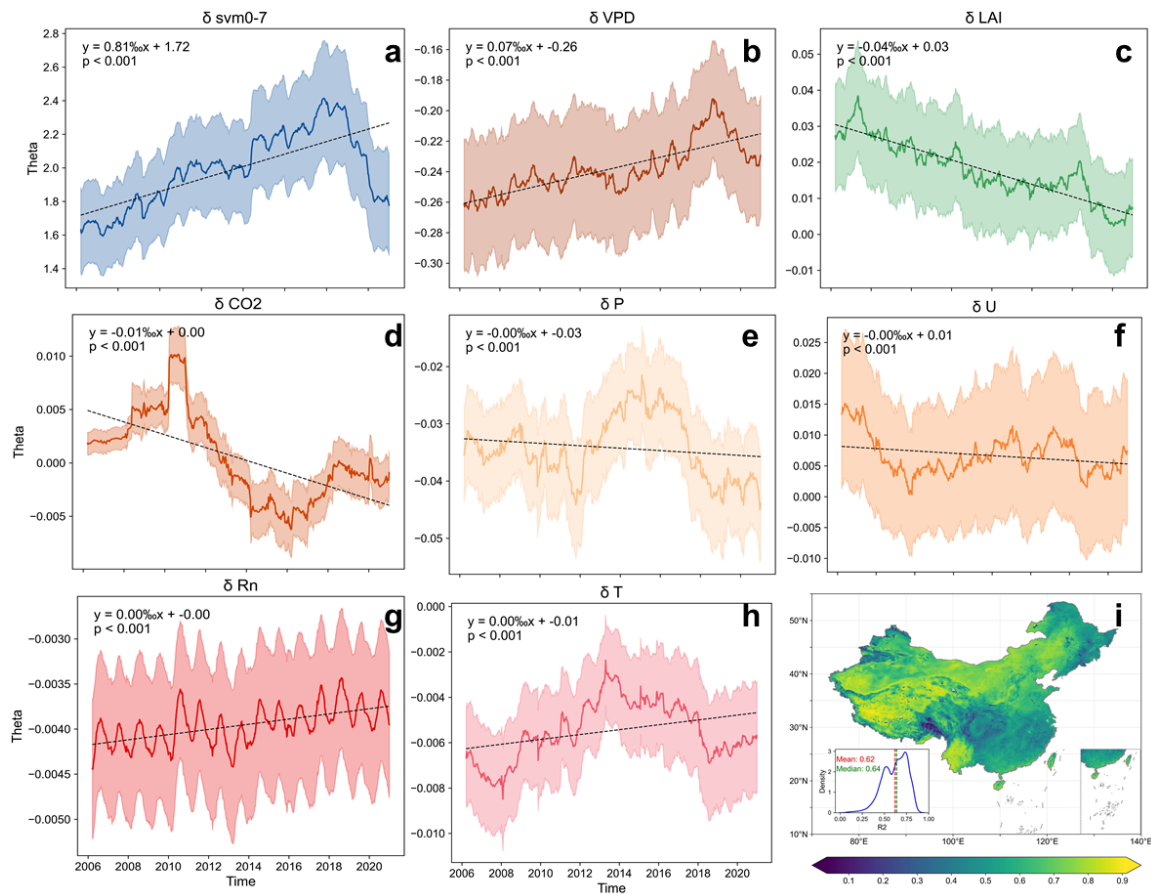
Figure S11. Sensitivity of the ESI to pivotal external drivers and its dynamic sensitivity trajectory. In accordance with Figs. 7c-e & S8, the sensitivity series was deduced using the Multiple Linear Regression (MLR) model with the following external drivers as inputs (R0): svm0-7, Rn, T, VPD, U, CO_2, and LAI. The temporal trend is analogous to that derived from MDLM, indicating an initial rise followed by a decline in θ_{svm}, with an aggregate significant increase of 0.81% d^{-1} (p<0.001). Concurrently, θ_{VPD} exhibited a significant overall rise of 0.07% d^{-1} (p<0.001), whereas θ_{LAI} displayed a notable decrease of -0.04% d^{-1} (p<0.001). The general trend directions for the remaining variables align with those observed in the MDLM outcomes (Fig. S8), which substantiates the robustness of the research discoveries and the efficacy of the MDLM approach. (i) The spatial distribution of the MLR model's coefficient of determination (R^2), with the red line denoting the mean (0.62) and the green line the median (0.64). This demonstrates that the model provides a high explanatory power, with the exception of the southwestern mountainous region.
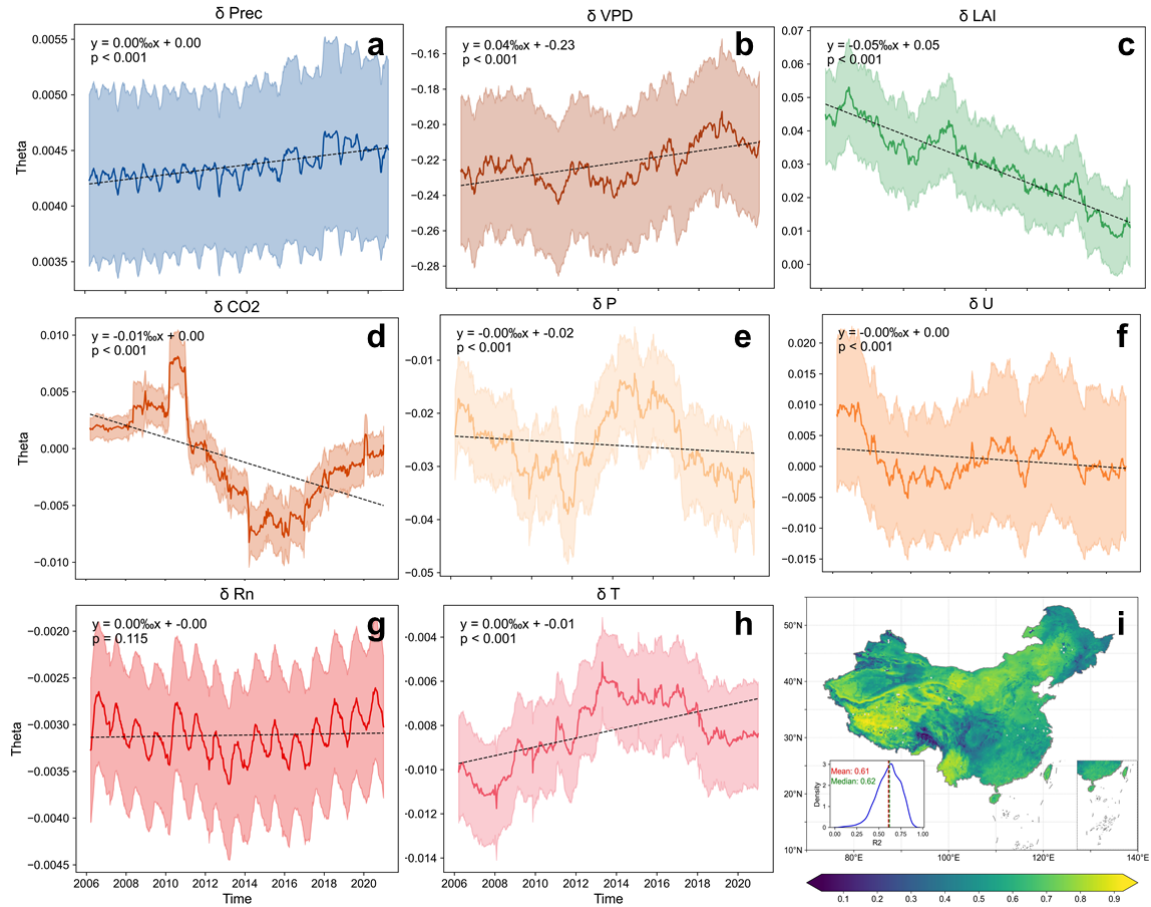
Figure S12. Sensitivity of the ESI to pivotal external drivers and its dynamic sensitivity trajectory. Same as Fig. S9 c-j, but the sensitivity is derived from the MLR model with the external driving factors input (R1): Prec, Rn, T, VPD, U, CO_2, and LAI. The trend directions of the variables are consistent with Figure S9, confirming the validity of the MLDM results. Additionally, the trend direction of b-h is consistent with Fig. S11, corroborating the robustness of the findings. (i) The distribution of decision coefficients R^2 across pixels reveals that both the mean (indicated by a red line at 0.61) and the median (indicated by a green line at 0.62) are below the goodness-of-fit values found in the R0 scenario. This indicates that, in the context of ESI fluctuations, precipitation as a source of water supply offers less explanatory power than soil moisture.
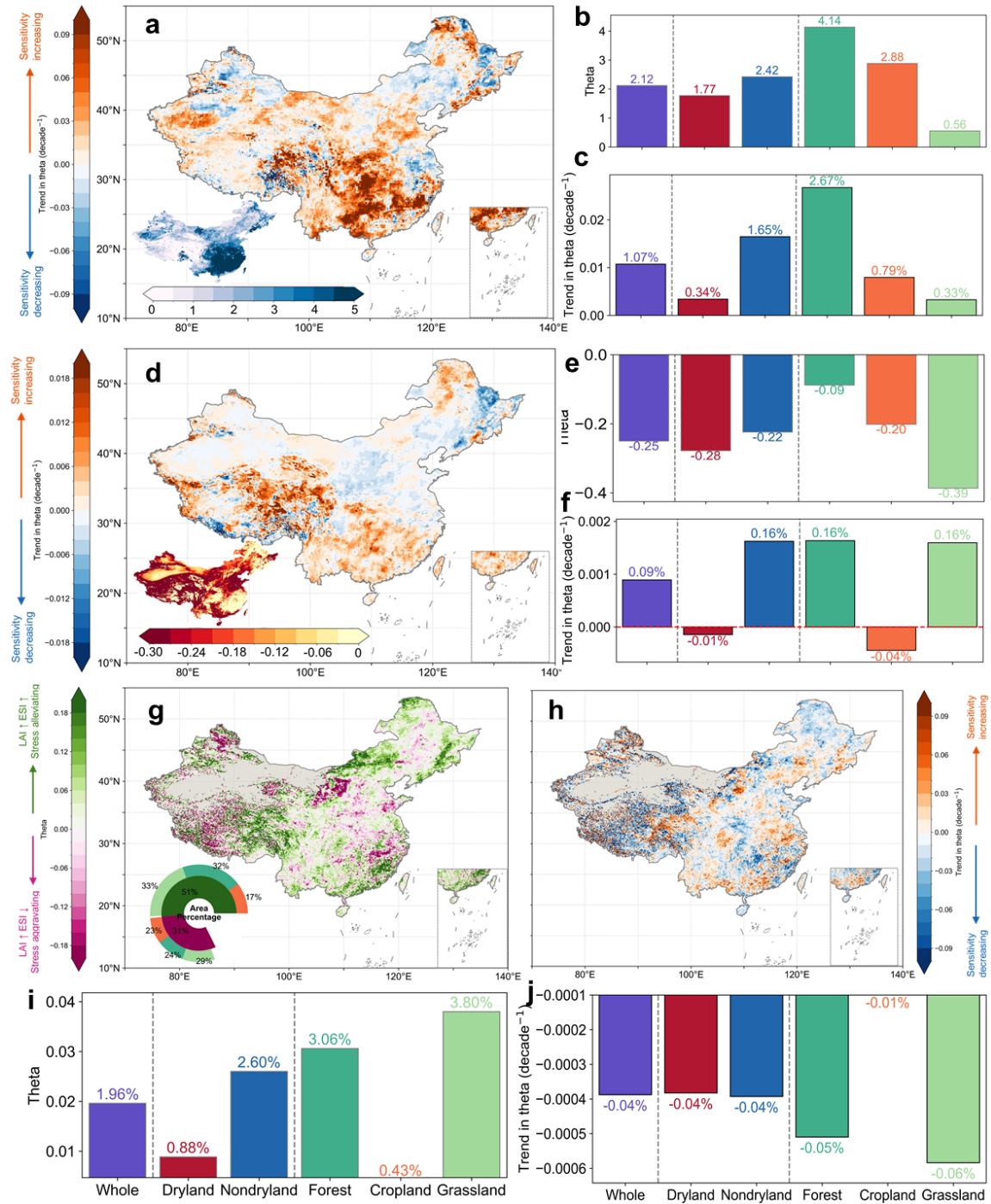
Figure S13. Spatiotemporal heterogeneity in svm0-7, VPD, and LAI sensitivity. Same as Fig. S9c-j, but the sensitivity is derived from the MLR model with the external driving factors input (R0): svm0-7, Rn, T, VPD, U, CO_2, and LAI. Given that the MLR model generates an averaged sensitivity series within a 5-year moving window, and the MLDM produces time-specific sequences, the figure is not numerically comparable to Figure 8. Instead, it serves to contrast the spatial distribution patterns and relative magnitudes across different categories. The patterns for $\boldsymbol{\theta_{svm}}$ and $\boldsymbol{\theta_{VPD}}$ depicted in figures (a-f) are consistent with Fig. 8, affirming the results' robustness. While the distributions in (g) and (h) resemble those in Fig. 8, notable disparities are present in the Tibetan Plateau and areas south of the Yangtze River's middle and lower reaches. (i) displays greater sensitivity in humid regions compared to arid ones, diverging

from the findings of Fig. 8i. Moreover, (j) does not reveal any differences between dry and humid regions but indicates a more pronounced trend in grasslands than in forests, deviating from Fig. 8j. Consequently, investigations into the interplay between moisture, climate, and vegetation in relation to vegetation change response might require consideration of temporal scale variations.
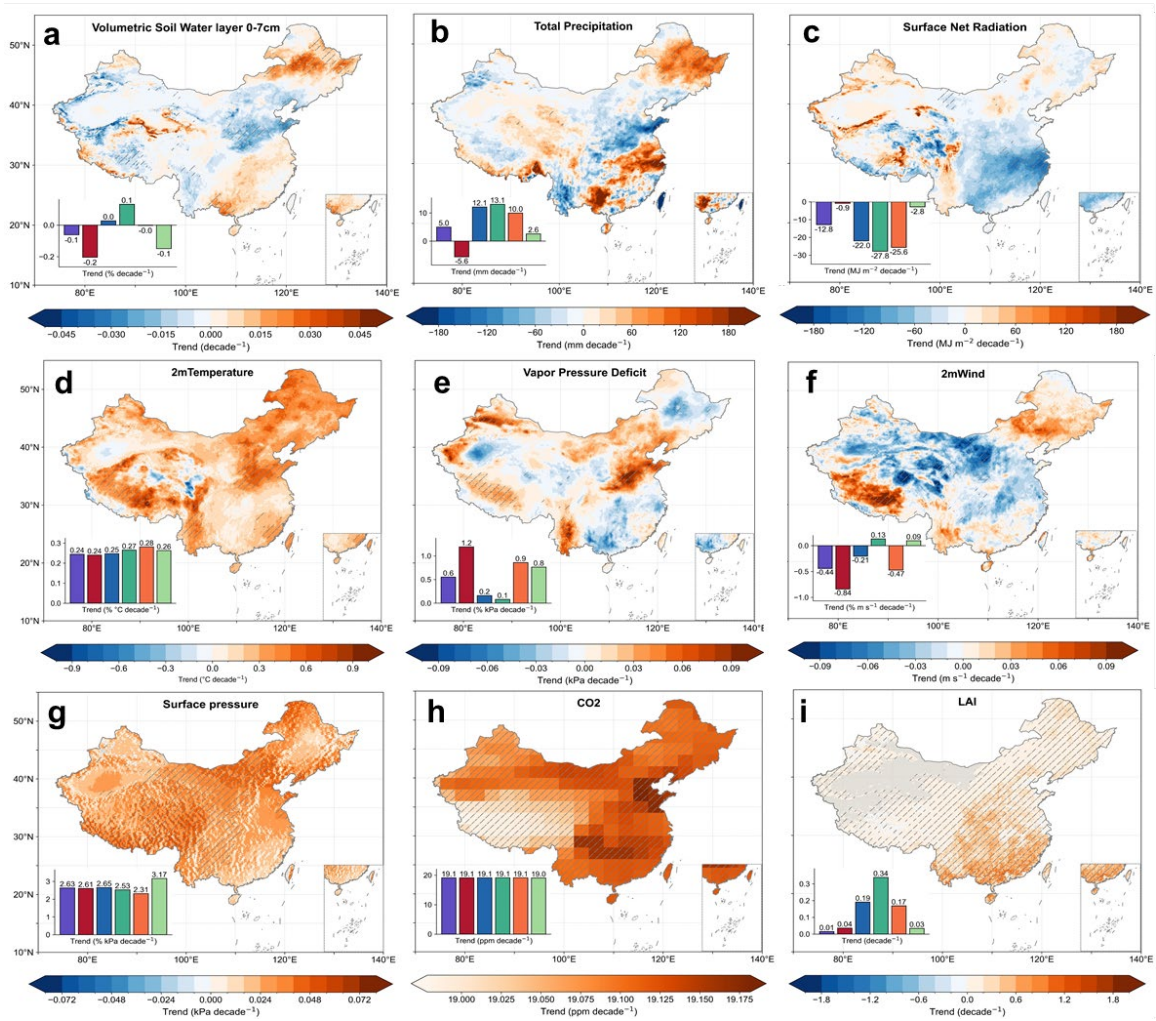
Figure S14. Spatiotemporal patterns of regional hydrological, meteorological, and vegetation variables over the period from 2001 to 2020. (a) Surface soil water at 0-7 cm depth (svm0-7); (b) total precipitation (Prec); (c) net radiation (Rn); (d) air temperature at 2m (T); (e) Vapor Pressure Deficit (VPD); (f) wind speed at 2m (U); (g) atmospheric pressure (P); (h) atmospheric CO_2 concentration; (i) Leaf Area Index (LAI).
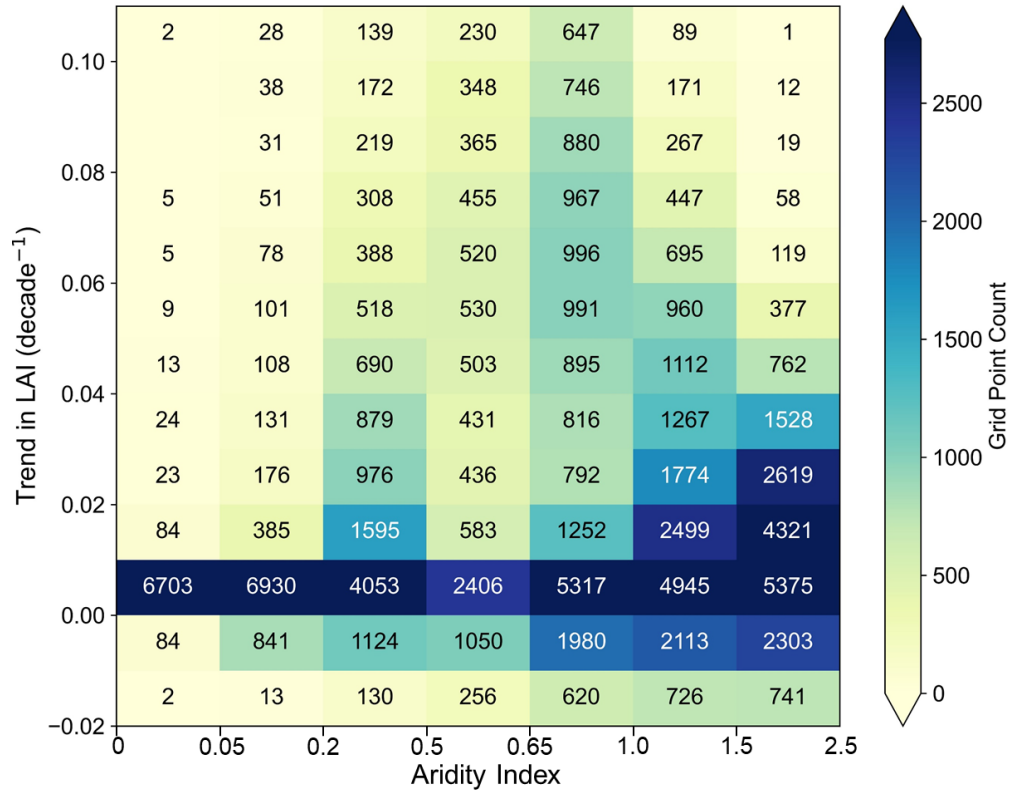
Figure S15. The number of grids in each bin grouped along the greening trend and aridity across mainland China.

Supplementary Tables

Table S1. Site characteristics of Eddy Covariance Flux Tower.

No.	Site Name	Lon (°E)	Lat(°N)	Vegetation Type (IGBP)	Altitude (m)	Duration	Source	Residual Energy (W/m²)	Reference
1	CBF	128.10	42.40	DBF	2180m	2003.01-2010.12	ChinaFlux	21.50	(Yu et al., 2006, 2008, 2014)
2	DXG	91.08	30.85	GRA	4400m	2004.01-2010.12		-15.65	
3	DHF	112.53	23.17	MF		2003.01-2010.12		15.90	
4	HBGS	101.33	37.67	GRA	3400m	2003.01-2010.12		2.09	
5	NMG	116.40	43.33	GRA		2004.01-2010.12		9.85	
6	QYF	115.07	26.73	ENF		2003.01-2010.12		15.14	
7	YCA	116.57	36.83	CRO	30m	2003.01-2010.12		6.46	
8	BNXF	101.27	21.90	CVM		2010.07-2014.12		23.85	(Yu et al., 2021)
9	HZF	121.02	51.78	DNF	773m	2014.01-2018.12		34.45	(Yan et al., 2023)
10	XLG	116.67	43.55	GRA	1250m	2006.01-2015.12		8.76	(Wang et al., 2023)
11	ALF	101.03	24.54	EBF	2400-2600m	2009.01-2013.12		12.20	(Qi et al., 2021)
12	ZOG	102.55	32.80	GRA	3500m	2015.06-2020.12		18.63	(Chen et al., 2023)
13	CLC	123.47	44.60	CRO	143	2018.06-2020.12		16.47	(Dong et al., 2023)
14	CN-Du2	116.28	42.05	GRA	1324m	2006.01-2008.12	FLUXNET	6.11	(Chen et al., 2009; Pastorello et al., 2020)
15	CN-Cng	123.50	44.58	GRA	171m	2007.01-2010.12		-0.60	
16	CN-Du3	116.28	42.06	GRA	1324m	2009.01-2010.12		19.73	(Pastorello et al., 2020)
17	CN-Sw2	111.90	41.79	GRA	1456m	2010.01-2012.12		12.96	
18	DZF	109.48	19.55	EBF	144m	2010.01-2018.12	Chinese Academy of Tropical Agricultural Sciences	22.74	(Yang et al., 2022)

							(CATAS)		
19	WSC	116.05	36.65	CRO	30m	2005.05-2006.09	(Tsinghua University) THU	13.26	(Lei and Yang, 2010a, b)
20	DSG	98.94	38.84	GRA	3739m	2015.01-2017.12	HiWATER	-42.08	(Che et al., 2019; Liu et al., 2011, 2016, 2018, 2023)
21	EJB	100.24	38.01	BSV	1054m	2015.06-2017.09		3.82	
22	HZB	100.32	38.76	BSV	1731m	2018.01-2020.12		-8.16	
23	EJM	101.13	41.99	MF	874m	2013.08-2017.12		-1.13	
24	JYG	101.11	37.84	GRA	3750m	2018.08-2020.12		4.38	
25	XYG	101.86	37.56	GRA	3616m	2019.04-2020.12	Cold and Arid Research Network of Lanzhou university (CARN)	10.79	(Changming Zhao and Renyi Zhang, 2021)
26	MQB	103.67	39.21	BSV	1020m	2019.08-2020.12		31.06	

According to the International Geosphere-Biosphere Programme (IGBP) classification, BSV = Barren Sparse Vegetation, CRO = Croplands, CVM = Cropland/Natural Vegetation Mosaics, DBF = Deciduous Broadleaf Forests, DNF = Deciduous Needleleaf Forests, EBF = Evergreen Broadleaf Forests, ENF = Evergreen Needleleaf Forests, GRA = Grasslands, MF = Mixed Forests, WET = Permanent Wetlands

Table S2. List of Variance Inflation Factor.

For each grid, collinearity tests were conducted on the anomaly series of variables across three temporal scales. The table lists the average values of the VIF (Variance Inflation Factor) for all grids, along with the 5th percentile (superscript) and the 95th percentile (subscript). Two scenarios, R0 and R1, have been established based on different combinations of input parameters to isolate and contrast the effects of soil moisture and precipitation.

Parameter Set: R0

Temporal resolution	svm0-7	Rn	T	VPD	U	P	CO_2	LAI
8day	$1.59_{2.14}^{1.20}$	$2.04_{3.18}^{1.09}$	$2.10_{3.32}^{1.34}$	$2.85_{4.15}^{1.87}$	$1.37_{2.03}^{1.06}$	$1.43_{1.98}^{1.07}$	$1.01_{1.02}^{1.00}$	$1.08_{1.23}^{1.01}$
16day	$1.64_{2.30}^{1.20}$	$2.05_{3.19}^{1.11}$	$2.14_{3.40}^{1.33}$	$3.00_{4.65}^{1.84}$	$1.43_{2.25}^{1.07}$	$1.40_{1.90}^{1.07}$	$1.01_{1.03}^{1.00}$	$1.11_{1.30}^{1.02}$
month	$1.67_{2.41}^{1.19}$	$2.09_{3.35}^{1.15}$	$2.27_{3.87}^{1.35}$	$3.16_{5.21}^{1.84}$	$1.54_{2.60}^{1.09}$	$1.42_{1.89}^{1.07}$	$1.01_{1.04}^{1.00}$	$1.15_{1.39}^{1.03}$

Parameter Set: R1

Temporal resolution	Prec	Rn	T	VPD	U	P	CO_2	LAI
8day	$1.85_{2.64}^{1.45}$	$2.30_{3.53}^{1.21}$	$2.28_{3.69}^{1.37}$	$2.96_{4.72}^{1.95}$	$1.38_{2.05}^{1.06}$	$1.01_{1.02}^{1.00}$	$1.45_{2.00}^{1.09}$	$1.05_{1.16}^{1.01}$
16day	$1.98_{3.01}^{1.49}$	$2.31_{3.54}^{1.18}$	$2.37_{4.28}^{1.37}$	$3.23_{5.73}^{1.99}$	$1.44_{2.28}^{1.07}$	$1.01_{1.02}^{1.00}$	$1.42_{1.92}^{1.09}$	$1.08_{1.24}^{1.01}$
month	$2.07_{3.32}^{1.46}$	$2.28_{3.60}^{1.17}$	$2.52_{5.13}^{1.37}$	$3.59_{6.73}^{2.09}$	$1.54_{2.62}^{1.09}$	$1.01_{1.03}^{1.00}$	$1.44_{1.92}^{1.08}$	$1.12_{1.35}^{1.02}$

Table S3. Interpretation of sensitivity obtained from Memory Dynamic Linear Model.

Absolute values of θ depict the evapotranspiration stress resistance to anomalies in each variable. Large absolute values indicate strong evapotranspiration stress responses to corresponding variable anomalies.

Classify	Description	Sign
Water-related Factors	θ_{svm}	*Positive* - Wetter conditions than average induce positive ESI anomalies, meaning that evaporative stress is alleviated.
	θ_{Prec}	
Vegetation-related Factors	θ_{LAI}	*Positive* - Denser and healthier vegetation conditions than average induce positive ESI anomalies, meaning that evaporative stress is alleviated.
Energy-related Factors	θ_{Rn}	*Negative* - Above-average thermal conditions induce negative ESI anomalies, meaning that evaporative stress is aggravated.
	θ_T	
Atmosphere-related Factors	θ_U	*Positive* - Faster wind speeds than average induce positive ESI anomalies, meaning that evaporative stress is alleviated.
	θ_{VPD}	*Negative* - More deficient atmospheric vapor pressure than average induce negative ESI anomalies, meaning that evaporative stress is aggravated.
	θ_P	*Negative* - Higher atmospheric pressure than average induce negative ESI anomalies, meaning that evaporative stress is aggravated.
	θ_{CO2}	*Negative* - Higher CO_2 concentration than average induce negative ESI anomalies, meaning that evaporative stress is aggravated.

References

Changming Zhao and Renyi Zhang: Cold and Arid Research Network of Lanzhou university (eddy covariance system of Guazhou station, 2020), https://doi.org/10.11888/Meteoro.tpdc.271477, 2021.

Che, T., Li, X., Liu, S., Li, H., Xu, Z., Tan, J., Zhang, Y., Ren, Z., Xiao, L., Deng, J., Jin, R., Ma, M., Wang, J., and Yang, X.: Integrated hydrometeorological, snow and frozen-ground observations in the alpine region of the Heihe River Basin, China, Earth Syst. Sci. Data, 11, 1483–1499, https://doi.org/10.5194/essd-11-1483-2019, 2019.

Chen, S., Chen, J., Lin, G., Zhang, W., Miao, H., Wei, L., Huang, J., and Han, X.: Energy balance and partition in Inner Mongolia steppe ecosystems with different land use types, Agricultural and Forest Meteorology, 149, 1800–1809, https://doi.org/10.1016/j.agrformet.2009.06.009, 2009.

Chen, W., Wang, S., and Niu, S.: A dataset of carbon, water and heat fluxes of Zoige alpine meadow from 2015 to 2020, China Scientific Data, 8, https://doi.org/10.11922/11-6035.csd.2023.0009.zh, 2023.

Dong, G., Wang, Y., Wang, K., Jiang, S., and Shao, C.: A dataset of carbon and water fluxes in the Changling alkali-saline paddy rice fields in the Songnen Plain, China (2018 –2020), China Scientific Data, 2023.

Lei, H. and Yang, D.: Interannual and seasonal variability in evapotranspiration and energy partitioning over an irrigated cropland in the North China Plain, Agricultural and Forest Meteorology, 150, 581–589, https://doi.org/10.1016/j.agrformet.2010.01.022, 2010a.

Lei, H. and Yang, D.: Seasonal and interannual variations in carbon dioxide exchange over a cropland in the North China Plain, Global Change Biology, 16, 2944–2957, https://doi.org/10.1111/j.1365-2486.2009.02136.x, 2010b.

Liu, S., Xu, Z. W., Wang, W. Z., Jia, Z. Z., Zhu, M. J., Bai, J., and Wang, J. M.: A comparison of eddy-covariance and large aperture scintillometer measurements with respect to the energy balance closure problem, Hydrol. Earth Syst. Sci., 15, 1291–1306, https://doi.org/10.5194/hess-15-1291-2011, 2011.

Liu, S., Xu, Z., Song, L., Zhao, Q., Ge, Y., Xu, T., Ma, Y., Zhu, Z., Jia, Z., and Zhang, F.: Upscaling evapotranspiration measurements from multi-site to the satellite pixel scale over heterogeneous land surfaces, Agricultural and Forest Meteorology, 230–231, 97–113, https://doi.org/10.1016/j.agrformet.2016.04.008, 2016.

Liu, S., Li, X., Xu, Z., Che, T., Xiao, Q., Ma, M., Liu, Q., Jin, R., Guo, J., Wang, L., Wang, W., Qi, Y., Li, H., Xu, T., Ran, Y., Hu, X., Shi, S., Zhu, Z., Tan, J., Zhang, Y., and Ren, Z.: The Heihe Integrated Observatory Network: A Basin-Scale Land Surface Processes Observatory in China, Vadose Zone Journal, 17, 1–21, https://doi.org/10.2136/vzj2018.04.0072, 2018.

Liu, S., Xu, Z., Che, T., Li, X., Xu, T., Ren, Z., Zhang, Y., Tan, J., Song, L., Zhou, J., Zhu, Z., Yang, X., Liu, R., and Ma, Y.: A dataset of energy, water vapor, and carbon exchange observations in oasis–desert areas from 2012 to 2021 in a typical endorheic basin, Earth Syst. Sci. Data, 15, 4959–4981, https://doi.org/10.5194/essd-15-4959-2023, 2023.

Pastorello, G., Trotta, C., Canfora, E., Chu, H., Christianson, D., Cheah, Y.-W., Poindexter, C., Chen, J., Elbashandy, A., Humphrey, M., Isaac, P., Polidori, D., Reichstein, M., Ribeca, A., Van Ingen, C., Vuichard, N., Zhang, L., Amiro, B., Ammann, C., Arain, M. A., Ardö, J., Arkebauer, T., Arndt, S. K., Arriga, N., Aubinet, M., Aurela, M., Baldocchi, D., Barr, A., Beamesderfer, E., Marchesini, L. B., Bergeron, O., Beringer, J., Bernhofer, C., Berveiller, D., Billesbach, D., Black, T. A., Blanken, P. D., Bohrer, G., Boike, J., Bolstad, P. V., Bonal, D., Bonnefond, J.-M., Bowling, D. R., Bracho, R., Brodeur, J.,

Brümmer, C., Buchmann, N., Burban, B., Burns, S. P., Buysse, P., Cale, P., Cavagna, M., Cellier, P., Chen, S., Chini, I., Christensen, T. R., Cleverly, J., Collalti, A., Consalvo, C., Cook, B. D., Cook, D., Coursolle, C., Cremonese, E., Curtis, P. S., D'Andrea, E., Da Rocha, H., Dai, X., Davis, K. J., Cinti, B. D., Grandcourt, A. D., Ligne, A. D., De Oliveira, R. C., Delpierre, N., Desai, A. R., Di Bella, C. M., Tommasi, P. D., Dolman, H., Domingo, F., Dong, G., Dore, S., Duce, P., Dufrêne, E., Dunn, A., Dušek, J., Eamus, D., Eichelmann, U., ElKhidir, H. A. M., Eugster, W., Ewenz, C. M., Ewers, B., Famulari, D., Fares, S., Feigenwinter, I., Feitz, A., Fensholt, R., Filippa, G., Fischer, M., Frank, J., Galvagno, M., et al.: The FLUXNET2015 dataset and the ONEFlux processing pipeline for eddy covariance data, Sci Data, 7, 225, https://doi.org/10.1038/s41597-020-0534-3, 2020.

Qi, D., FEI, X., SONG, Q., ZHANG, Y., SHA, L., LIU, Y., ZHOU, W., LU, Z., and FAN, Z.: A dataset of carbon and water fluxes observation in subtropical evergreen broad-leaved forest in Ailao Shan from 2009 to 2013, China Scientific Data, 6, https://doi.org/10.11922/csdata.2020.0089.zh, 2021.

Simoen, E., Papadimitriou, C., and Lombaert, G.: On prediction error correlation in Bayesian model updating, Journal of Sound and Vibration, 332, 4136–4152, https://doi.org/10.1016/j.jsv.2013.03.019, 2013.

Wang, Y., You, C., and Chen, S.: A dataset of carbon and water fluxes of mowing grasslands in Xilinhot, Inner Mongolia during 2006-2015, China Scientific Data, 2023.

Yan, Y., Zhou, G., Jia, B., Song, J., and Zhang, S.: A dataset of carbon and water fluxes of the boreal forest ecosystem in Huzhong (2014 – 2018), China Scientific Data, 2023.

Yang, S., Liu, J., Yang, C., Lan, G., Song, B., and Wu, Z.: A dataset of carbon and water fluxes and micrometerological elements in Danzhou rubber plantation (2010-2018), China Scientific Data, 2022.

Yu, G., Wen, X.-F., Sun, X.-M., Tanner, B. D., Lee, X., and Chen, J.-Y.: Overview of ChinaFLUX and evaluation of its eddy covariance measurement, Agricultural and Forest Meteorology, 137, 125–137, https://doi.org/10.1016/j.agrformet.2006.02.011, 2006.

Yu, G., Zhang, L., Sun, X., Fu, Y., Wen, X., Wang, Q., Li, S., Ren, C., Song, X., Liu, Y., Han, S., and Yan, J.: Environmental controls over carbon exchange of three forest ecosystems in eastern China, Global Change Biology, 14, 2555–2571, https://doi.org/10.1111/j.1365-2486.2008.01663.x, 2008.

Yu, G., Chen, Z., Piao, S., Peng, C., Ciais, P., Wang, Q., Li, X., and Zhu, X.: High carbon dioxide uptake by subtropical forest ecosystems in the East Asian monsoon region, Proc. Natl. Acad. Sci. U.S.A., 111, 4910–4915, https://doi.org/10.1073/pnas.1317065111, 2014.

Yu, H., QI, D., ZHANG, Y., SHA, L., LIU, Y., ZHOU, W., DENG, Y., and SONG, Q.: An observation dataset of carbon and water fluxes in Xishuangbanna rubber plantations from 2010 to 2014, China Scientific Data, 6, https://doi.org/10.11922/csdata.2020.0090.zh, 2021.

Zhang, E. L., Feissel, P., and Antoni, J.: A comprehensive Bayesian approach for model updating and quantification of modeling errors, Probabilistic Engineering Mechanics, 26, 550–560, https://doi.org/10.1016/j.probengmech.2011.07.001, 2011.